Title: Nondestructive atomic compositional analysis of BeMgZnO quaternary alloys using ion beam analytical techniques

Author: Z. Zolnai M. Toporkov J. Volk D.O. Demchenko S. Okur Z. Szabó Ü. Özgür H. Morkoç V. Avrutin E. Kótai

PII: S0169-4332(14)02540-9
DOI: http://dx.doi.org/doi:10.1016/j.apsusc.2014.11.067
Reference: APSUSC 29112

To appear in: *APSUSC*

Received date: 9-6-2014
Revised date: 11-11-2014
Accepted date: 11-11-2014

Please cite this article as: Z. Zolnai, M. Toporkov, J. Volk, D.O. Demchenko, S. Okur, Z. Szabó, Ü. Özgür, H. Morkoç, V. Avrutin, E. Kótai, Nondestructive atomic compositional analysis of BeMgZnO quaternary alloys using ion beam analytical techniques, *Applied Surface Science* (2014), http://dx.doi.org/10.1016/j.apsusc.2014.11.067

Nondestructive atomic compositional analysis of BeMgZnO quaternary alloys using ion beam analytical techniques

Z. Zolnai[1,*], M. Toporkov[2], J. Volk[1,2], D. O. Demchenko[3], S. Okur[2], Z. Szabó[1], Ü. Özgür[2], H. Morkoç[2], V. Avrutin[2], and E. Kótai[4]

[1]Research Centre for Natural Sciences, Institute of Technical Physics and Materials Science (MFA), H-1121 Budapest, Konkoly-Thege M. út 29-33, Hungary

[2]Department of Electrical and Computer Engineering, Virginia Commonwealth University, 601 W Main St, Richmond, VA 23284, USA

[3]Department of Physics, Virginia Commonwealth University, 701 W. Grace St., Richmond, VA 23284, USA

[4]Wigner Research Centre for Physics, Institute for Particle and Nuclear Physics, H-1121 Budapest, Konkoly-Thege M. út 29-33, Hungary

*****Corresponding author e-mail: zolnai.zsolt@ttk.mta.hu*

PACS numbers: 79.20.Rf, 61.72.uj, 71.55.Gs, 71.15.Mb

Keywords: BeMgZnO alloy; Ion beam analysis; Proton elastic backscattering; Tauc bandgap; Density functional theory (DFT); Bandgap engineering

Highlights

BeMgZnO thin layers were grown with plasma assisted molecular beam epitaxy (MBE)

The Be contents were accurately measured with RBS and proton elastic backscattering

The Tauc bandgap was measured from optical transmittance experiments

The bandgap has been varied between 3.26 eV and 4.62 eV via the Be and Mg content

Experimental and density functional theory calculated bandgaps were in good agreement

Abstract

The atomic composition with less than 1-2 atom % uncertainty was measured in ternary BeZnO and quaternary BeMgZnO alloys using a combination of nondestructive Rutherford backscattering spectrometry with 1 MeV He^+ analyzing ion beam and non-Rutherford elastic backscattering experiments with 2.53 MeV energy protons. An enhancement factor of 60 in the cross-section of Be for protons has been achieved to monitor Be atomic concentrations. Usually the quantitative analysis of BeZnO and BeMgZnO systems is challenging due to difficulties with appropriate experimental tools for the detection of the light Be element with satisfactory accuracy. As it is shown, our applied ion beam technique,

supported with the detailed simulation of ion stopping, backscattering, and detection processes allows of quantitative depth profiling and compositional analysis of wurtzite BeZnO/ZnO/sapphire and BeMgZnO/ZnO/sapphire layer structures with low uncertainty for both Be and Mg. In addition, the excitonic bandgaps of the layers were deduced from optical transmittance measurements. To augment the measured compositions and bandgaps of BeO and MgO co-alloyed ZnO layers, hybrid density functional bandgap calculations were performed with varying the Be and Mg contents. The theoretical vs. experimental bandgaps show linear correlation in the entire bandgap range studied from 3.26 eV to 4.62 eV. The analytical method employed should help facilitate bandgap engineering for potential applications, such as solar blind UV photodetectors and heterostructures for UV emitters and intersubband devices.

1. Introduction

ZnO and related materials have attracted considerable attention owing to their promising optical and electrical properties for a variety of optoelectric devices, including light emitting diodes and solar-blind UV detectors [1]. For solar-blind UV absorption the cut-off wavelength should be below 280 nm (4.5 eV) [1-3] corresponding to a significantly larger bandgap than that of ZnO (3.37 eV). Alloying ZnO with MgO, which is reasonably traditional, leads to the ternary compound MgZnO [4, 5] with tunable bandgap up to 4.55 eV in wurtzite phase [6]. However, alloys with high band gap values are obtained using low growth temperatures of the order of 250 ^{o}C with very inferior crystalline quality. Unfortunately, use of nominal high temperatures for attaining quality material, the bandgap tuning is limited because of phase segregation for Mg contents above ~33% induced by structural mismatch between the wurtzite ZnO and rock salt MgO [7]. To overcome this limitation, quaternary BeMgZnO has been proposed [1, 8, 9]. As initial experiments and theoretical studies revealed, co-alloying of ZnO together with BeO and MgO results in more stable wurtzite structure, i.e. void of phase separation, as compared to ternary MgZnO or BeZnO alloys. For certain growth conditions quaternary layers with sufficiently large bandgaps up to 4.9 eV [8] have been achieved. Theoretical studies of bandgap variation and equilibrium lattice parameters for the quaternary BeMgZnO system have been performed mainly using density functional theory (DFT), known to significantly underestimate the bandgap [10, 11]. In addition, comparison of theory with experiment has been problematic due to difficulties with appropriate experimental tools for Be and Mg concentration analysis with satisfactory accuracy, particularly that of Be which is rather difficult to detect.

Recently Be depth distribution in BeZnO alloys has been revealed by SIMS [12]. Although sputter depth profiling is a powerful technique, it is destructive; and sputtering itself produces a range of artifacts and alters the sample. Moreover, SIMS needs to be quantified by standards because the results are extensively affected by matrix effects. Hence, the absolute measurement of Be contents by SIMS is challenging.

Another method often applied for Be analysis in Be-alloyed ZnO and MgZnO is X-ray photoelectron spectroscopy (XPS) [1, 3, 12]. In XPS, the atomic composition may be calculated from the photoelectron peak intensities of different elements. In this procedure, both the photoelectric cross-section (σ) and the inelastic mean free path (IMFP) of the photoelecrons from each element of the layer is required. In general, IMFP data can be considered with an uncertainty of about 12% on average, while σ values are scattered within 5-15 % , respectively [13]. For multi-elemental targets, like BeMgZnO, however, the IMFP data usually have much higher uncertainty for the different constituents. Therefore, it is rather difficult to determine the precise Be content by XPS in BeMgZnO due to the significantly large uncertainties in detecting the light Be element [3]. Moreover, the depth profiling XPS

methods suffer from similar problems as the SIMS technique. Due to such limitations, the Be content after sample preparation is sometimes given by an effective parameter, e.g. the number of laser pulses ablated on BeO target during the pulsed laser deposition (PLD) of BeMgZnO layers [8] or cell temperature during molecular beam epitaxy (MBE) growth [14]. Such descriptions lack the specificity needed for direct quantitative comparison of theory and experiment in engineering and understanding the structural and optical properties of BeZnO and BeMgZnO alloys.

In this work, we employed ion beam analysis (IBA) instead which is a powerful and nondestructive characterization tool for BeMgZnO. IBA allows accurate measurements of concentrations of constituents and the stoichiometry of thin films as a function of depth. Also, its capability in determining the shape and the size of nanostructures has been demonstrated [15, 16]. Recently an assertion of 1% absolute accuracy for Rutherford Backscattering Spectrometry (RBS) – the simplest IBA method – has been validated on the basis of the uncertainty budget [17]. However, the sources of uncertainty in evaluation always (also in this work) depend on the properties of the material system to be analyzed and the given measurement conditions. Usually the detection of light elements in the presence of heavier ones is especially challenging in RBS experiments. In such cases chemical analysis of light elements in binary, ternary, or quaternary compounds becomes feasible with IBA when e.g. applying resonances which appear in the elastic backscattering cross-section at characteristic energies of the analyzing He^+ or H^+ ions. For instance, the carbon sublattice of SiC can be investigated with six [18] or even 120 times [19] higher sensitivity by 3.55 MeV and 4.26 MeV He^+ ion beams, respectively, as compared to RBS performed in the 1-2 MeV energy range where the cross-section is given by the Rutherford value for carbon.

In the case of Be containing ZnO and MgZnO, a strong resonance with an enhancement factor of 60(±3) appears in the elastic backscattering cross-section of the $^{9}Be(p,p)^{9}Be$ reaction for proton energies around 2.5 MeV [20, 21]. Although the concept of monitoring Be with this reaction was proposed and applied for BeZnO [22], actually there has been no experimental demonstration with a detailed analysis of the measured backscattering spectra. Note that the resonance-enhanced non-Rutherford cross-sections for the $^{nat}Mg(p,p)^{nat}Mg$ and $^{16}O(p,p)^{16}O$ elastic backscattering reactions also have to be considered in such spectrum evaluation procedures for BeMgZnO alloys.

In this work, data obtained from RBS with He^+ ions (He^+-RBS) and from non-Rutherford elastic backscattering spectrometry with protons (p-EBS) were analyzed together utilizing the well-established RBX spectrum simulation code [23]. Details on the simulation of backscattering spectra in the presence of sharp resonances and a recent intercomparison of ion beam analysis softwares including RBX can be found elsewhere [24-26]. With the He^+-RBS/p-EBS combined IBA technique the composition and layer structure of wurtzite BeZnO/ZnO and BeMgZnO/ZnO systems grown on (0001) sapphire were determined with good accuracy down to Be content of 7 atom% (with typical uncertainty of ±1-2 atom%).

The bandgaps of the analyzed layers were estimated with hybrid density functional theory calculations. In the model the supercells were constructed with the Be and Mg concentrations taken from the evaluation of He^+-RBS and p-EBS spectra. The theoretical bandgaps show linear correlation with the experimental optical bandgaps for different Be and Mg contents. The observed offset can be reasonably related to fundamental material properties and to the features of the applied hybrid functional method.

2. Experiments

Six quaternary BeMgZnO (samples Q1-Q6), one ternary BeZnO (T), as well as a ZnO reference thin films were grown on (0001) sapphire substrates using plasma assisted

molecular beam epitaxy (MBE) with an RF oxygen plasma source and Knudsen cells for Be, Mg, and Zn. Pyrolytic Boron Nitride (PBN) crucibles were used for Mg and Zn sources and a BeO crucible for the Be source. First, a 2 nm-thick MgO buffer layer was grown for each sample at 750°C to avoid 30° rotation domains and ensure 2D nucleation. Subsequently, a ~10-20 nm-thick low-temperature ZnO buffer layer was grown at 300°C and annealed at 750°C to achieve an atomically flat surface. The same annealed buffer layers were overgrown by different layer compositions (Q1-Q6, T, and ZnO) at a substrate temperature of around 400°C. To vary the $Be_xMg_yZn_{1-x-y}O$ composition, the Mg source temperature was changed between 416 °C and 452 °C, the Be source temperature was set to either 1150°C or 1170 °C while the Zn source temperature was varied between 317°C and 324°C.

The out-of-plane *c* and in-plane *a* lattice parameters of the BeZnO and BeMgZnO layers were derived from X-Ray Diffraction (XRD) measurements for the symmetric (0002) and skew-symmetric (10-13) reflections, respectively, using the line focus mode. Further details about growth and characterization can be found in Ref. [27]. The optical bandgap (E_g) of $Be_xZn_{1-x}O$ and $Be_xMg_yZn_{1-x-y}O$ alloys were deduced from optical transmittance measurements carried out in the 200-1100 nm wavelength range using an Agilent 8453 spectrophotometer.

The 1 MeV He^+-RBS and 2.53 MeV p-EBS experiments were performed with the 5 MV Van de Graaff accelerator of the Institute for Particle and Nuclear Physics of the Wigner Research Centre for Physics in Budapest, Hungary. The sample chamber pressure during experiments was 1.2×10^{-4} Pa. To reduce the hydrocarbon deposition, liquid N_2 cooled traps were used along the beam path and around the wall of the chamber. During the actual measurements, the beam was collimated to dimensions of 0.5×0.5 mm^2, while the beam divergence was kept below 0.06°. Typically, a beam current of ~20 nA was measured by transmission Faraday cup [28]. Backscattered He^+ and H^+ ions were detected using an ORTEC surface barrier detector mounted in the Cornell geometry at a scattering angle of $\Theta = 165°$. A blind detector with Al reflection layer on top was used to eliminate background counts from ion beam-induced luminescence of the epilayers and of the underlying substrate. The energy resolution of the detection system was 20 keV. To avoid yield variations due to axial or planar channeling of the analyzing ions in the single-crystalline epilayers and in the sapphire substrate random spectra were recorded in each measurement via off-tilting the sample surface normal by an angle of $\alpha = 7°$ with respect to the incoming ion beam. The random orientation conditions were achieved using a two-axis goniometer system capable of determining the target orientation to a precision of 0.01° and 0.1° in tilt and azimuthal angles, respectively. To increase the accuracy of evaluation, spectra were also recorded at tilt angles of $\alpha = 45^o$ and $\alpha = 70^o$ for He^+-RBS and p-EBS analysis, respectively. In the latter case the peak intensity for Be can be increased by a factor of 2.9 according to $1/\cos(\alpha)$ [16].

Detailed spectrum analysis, which takes into account the exact measurement geometry (Cornell configuration, scattering angle, detector solid angle, sample tilt angle), energy dependence of the elastic scattering cross-section and inelastic stopping cross-section in the target, energy straggling contributions in the sample and in the detection system, has been performed using the RBX spectrum simulation code [23]. The spectrum evaluation has been performed as an iterative manual procedure treating a set of spectra in turn until self-consistency has been achieved between the He^+-RBS and p-EBS spectra recorded on the same sample at different tilt angles. In the evaluation, the Rutherford cross-section data for He^+ backscattering were considered, while the non-Rutherford elastic proton backscattering cross-section data for Be [20, 21, 29], O [30, 31], Mg [32], and Al [33-35] were adopted from the literature. Note for Be data from Leavitt [21] and data from Mashkarov [29] agree well within

the Leavitt's experimental uncertainty of 5% in the energy range of interest (~2500-2530 keV). For Al the data in Refs. [33] and [35] were reported for a scattering angle of 170^o while in Ref. [30] for 160^o, respectively. However, as one can check they are practically equal in all three reports. In the case of Zn, the Rutherford value [36] was used within the full energy range for proton backscattering. It can be emphasized that significant recent efforts have been performed in the evaluation of p-EBS cross-sections [37-39] and the evaluated data from SigmaCalc are also given in the Ion Beam Analysis Nuclear Data Library (IBANDL) database [40]. Nevertheless, in this work the measured p-EBS cross-sections were used for convenience as they are indistinguishable from the evaluated ones at the accuracy of the analysis.

In the hybrid density functional theory calculations the input concentration values for x and y in $Be_xMg_yZn_{1-x-y}O$ were adopted from the evaluation of the He^+-RBS and p-EBS spectra. The calculations were performed using Heyd-Scuseria-Ernzerhof (HSE) [40] hybrid functional implemented in the VASP code [42], with projector augmented wave method (PAW) [43, 44]. In a HSE hybrid functional calculation the electron exchange interactions are separated into the short- and long-range contributions. The slowly varying long-ranged exchange is computed using generalized gradient approximation (GGA) to the DFT. The short-range exchange is computed as a mixture of GGA and Fock-type exchange. It is also often useful to tune the amount of Fock exact exchange for a particular material in order to obtain the best agreement of computed band gap with experiment. We use exchange tuned HSE hybrid functional, where the amount of exact exchange is set to be 37.5%. The exchange range separation parameter in HSE was kept at 0.2 Å^{-1}. The resulting bulk ZnO bandgap of 3.43 eV is in excellent agreement with low temperature experimental value of E_g = 3.436 eV considering the measured excitonic bandgap of 3.376 eV [45] and the large exciton binding energy of 60 meV for ZnO [46]. It is worth noting that HSE calculations do not include any temperature effects. All alloy calculations were performed in supercells with 72 atoms and using Γ–point eigenvalues only. All atomic structures were relaxed at the GGA level with respect to the lattice parameters a and c, a/c ratio, and all internal degrees of freedom, including the wurtzite internal parameter u, to yield forces of 0.01 eV/Å or less. The planewave basis sets with 500 eV energy cutoff were used in GGA calculations. This allowed accurate calculations of the BeMgZnO crystal structure within systematic GGA errors. The electronic properties were then computed for relaxed lowest energy structures using exchange tuned HSE hybrid functional calculations with 400 eV energy cutoff. In principle, three different basic binary compounds ZnO, BeO, and MgO could have three different exchange tuning parameters that recover experimental bandgap. Therefore, it could be problematic to use a common exchange tuning scheme for a quaternary compound containing all four elements. However, bulk band gap of BeO computed with the same Fock exchange ratio of 37.5% is 10.2 eV, which is reasonably close to the experimental value of 10.6 eV [47, 48]. The wurtzite structure of MgO is thermodynamically unstable, which makes it difficult to directly estimate the errors in a bandgap of Mg containing oxide alloy. However, computed bandgap for the stable rock-salt phase of MgO with the same amount of exchange is 7.72 eV, while measured gap is 7.83 eV [49]. This allows us to use the same value for the Fock exchange fraction with expectation that reasonable bandgaps can be obtained at intermediate concentrations of Mg and Be in BeMgZnO, because all bulk bandgaps are in good agreement with experiment.

3. Results and discussion

Fig. 1 shows the elastic backscattering cross-sections (σ) of Be [29], O [31], Mg [32], Al [33, 34], and Zn [36] elements for He^+ and H^+as a function of the ion energy, used in the RBX spectrum evaluation procedure. Note the Al atoms are present in the sapphire substrate only while oxygen atoms are present in sapphire, in the buffer ZnO layer, and in the BeZnO and BeMgZnO layers, too. For He^+ analysis σ is given by the Rutherford value (σ_R) which is proportional to $\sim Z^2$, the atomic number of the target atom, and therefore, the Be cross-section is negligible as compared to that of Zn, and significantly lower as compared to those of Al, Mg, and O. For H^+ analysis, however, except for Zn, σ deviates from the Rutherford value for all the investigated elements due to nuclear resonances. For Be an enhancement factor of ~60 can be observed (Table I); and therefore, $\sigma(Be)$ becomes comparable to $\sigma(Zn)$ and is much higher than $\sigma(Al)$, $\sigma(Mg)$, and $\sigma(O)$ for ~2.5 MeV protons. Accordingly, the quantitative analysis of Be in BeZnO and BeMgZnO becomes possible in p-EBS experiments. Note that in Fig. 1(b) the cross-sections for O, Mg, and Zn vary smoothly with energy while the Al curve exhibits strong oscillations. All these features must be taken into consideration in the simulation of p-EBS spectra in order to accomplish Be content analysis with good accuracy.

Gray stripes in Fig. 1 show the energy lost by the He^+ and H^+ projectiles through inelastic electronic stopping when they cross a 150 nm-thick ZnO layer. The energy losses were calculated by SRIM simulations [50] assuming a mass density of 5.6 g cm^{-3} for ZnO. For H^+ the energy loss is negligible and hence the analysis has poor depth resolution. In comparison, significant amount of energy is lost for He^+ due to the higher electronic stopping power, S_e, see Table 1. Consequently, depth profiling and layer thickness measurement with 1 MeV He^+ becomes accessible.

Fig. 2(a) shows typical 1 MeV He^+-RBS spectra of ZnO, BeZnO, and BeMgZnO layers. The different widths of the Zn spectra correspond to different layer thicknesses as indicated by the depth scale for Zn. Distinct Zn spectrum heights indicate the variation of the Zn concentration in the different samples. Mg contents, e.g., for Q3 and Q4, can be estimated from the plateau heights between channels 120-140. However, the Be signal cannot be detected due to the low Rutherford cross-section and large Al and O background for Be. Also, the surface edge for Be is located at low energy close to the detection limit because of the low kinematic factor [36], $K = 0.15$, of the He^+ ions for Be. In summary, from He^+-RBS analysis the layer thicknesses and the Zn and Mg concentration depth profiles can be evaluated but the Be content can only be deduced indirectly.

The measured p-EBS spectrum of one of the BeMgZnO layers (sample Q2) and the corresponding RBX simulation are compared in Fig. 2(b) for the sample tilt angle of $\alpha = 7^o$. Despite oscillations in the Al cross-section there is a clear agreement in the full energy range. The sharp peak at channel #325 originates from the spike in $\sigma(Al)$ at a proton energy of ~2485 keV while the bumps between channels #100-220 are due to other oscillations of $\sigma(Al)$ at lower proton energies (see Fig. 1(b)). We emphasize that the Be peak is situated on a large background from Al_2O_3. Therefore, the good measurement statistics and the quality of the spectrum fit are the prerequisites for an accurate Be analysis.

There is a striking difference between the spectra in Fig. 2(a) and (b): the He^+-RBS spectrum is dominated by the BeMgZnO yield, while the p-EBS spectrum mostly originates from the substrate Al_2O_3 signal. The main reasons are the one order of magnitude difference in the electronic stopping power, S_e, of He^+ and H^+, and the strong enhancement in the cross-section of oxygen for protons with respect to the Rutherford value, see Table 1. Due to low mass of protons, the kinematic factor for Be is $K = 0.64$, and thus the Be signal is detected at high channel numbers around #250 in Fig. 2(b). Because the p-EBS method has no considerable depth resolution in BeMgZnO, the Zn and Be signals provide integral peak

intensities proportional to both the BeMgZnO layer thickness and the Zn and Be concentrations.

The inset in Fig. 2(b) shows the schematic of the experiment and the sample structure used in RBX spectrum evaluation. In the spectrum simulation procedure the following parameters were varied: (*i*) the thickness of the buffer ZnO layer (*ii*) the thickness of the BeMgZnO layer (both in units of atom cm^{-2} following the convention of thickness measurement in RBS analysis), and (*iii*) the compositional contents *x, y* in $Be_xMg_yZn_{1-x-y}O$. The substrate was correctly considered as stoichiometric Al_2O_3. The parameters (*i*), (*ii*), and (*iii*) have been varied to achieve the sample structure which simultaneously fits both the He^+-RBS and p-EBS spectra for all sample tilt angles. Depth scales for the spectra were determined by appropriate energy-to-depth conversion considering energy dependent stopping of He^+ or H^+ in the RBX program. Evaluated layer thicknesses were converted from units of *atom* cm^{-2} to units of *nm* assuming a mass (atomic) density of $\rho = 5.6$ g cm^{-3} ($N = 8.29\times10^{22}$ atom cm^{-3}) for ZnO. The atomic densities for BeZnO and BeMgZnO were corrected using the *c*-axis parameters obtained from XRD data, shown in Table 2.

Fig. 3 shows the He^+-RBS spectra of ZnO, BeZnO (sample T), and two BeMgZnO layers (Q3 and Q5) recorded for sample tilt angles of 7^o and 45^o, respectively. RBX simulations are also shown with green and red lines. The height of the Zn spectrum for pure ZnO provides the reference level. Substitution of Zn atoms by Mg and Be atoms results in a clearly observable decrease in Zn plateau heights. For the BeZnO sample (T), the decrease of about 8% is indicative of a $Be_{0.08}Zn_{0.92}O$ alloy. The verification of the Be content is given by the corresponding p-EBS spectra (not shown). For the BeMgZnO sample Q3 the significant drop of the Zn yield in Fig. 3(a) is accompanied by the appearance of the Mg signal at channel #145 with a plateau toward lower energies. From the plateau height, the amount of Mg substituting Zn can be estimated. In addition to substitution of the Zn atoms by Mg, additional substitution of Zn by Be has to be considered in the fitting procedure to reconstruct the height of both the Zn and Mg signals for Q3. The accurate Be content in sample Q3 is evaluated from the p-EBS spectra shown in Fig. 4(a) and with a magnified Be peak region in Fig. 5(b). Here the simultaneous fit of the He^+-RBS and p-EBS spectra gives the $Be_{0.07}Mg_{0.33}Zn_{0.60}O$ composition, see Table 2. Compared to Q3, the Zn yield drops even further for sample Q5 in Fig. 3(b). This feature is the consequence of the higher Mg yield in Fig. 3(b), and the more intense Be peak in Fig. 5(c). For Q5 multiple RBX spectra fit results in the composition $Be_{0.19}Mg_{0.42}Zn_{0.39}O$, see Table 2. Note, for samples Q1, Q2, Q4, and Q6 atomic compositions of $Be_{0.11}Mg_{0.14}Zn_{0.75}O$, $Be_{0.08}Mg_{0.30}Zn_{0.62}O$, $Be_{0.07}Mg_{0.46}Zn_{0.47}O$, and $Be_{0.12}Mg_{0.52}Zn_{0.36}O$ were obtained, respectively.

In Fig. 3 the yield increase at the low energy side of the Zn spectrum for samples Q3 and Q5 is caused by the stoichiometry change when crossing the interface between the BeMgZnO and the underlying thin ZnO buffer layer. Such step is not seen for pure ZnO and for BeZnO because of zero and only 8% deficiency in the Zn content compared to the buffer ZnO layer, respectively. Also, there is no stoichiometry change within the BeMgZnO layers in Fig. 3, indicating homogeneous layer growth as a function of time. For samples Q1-Q6 the buffer layer thickness can be evaluated from He^+-RBS analysis, see Table 2. In He^+-RBS measurements, when tilting the sample from $\alpha = 7^o$ to 45^o, the Zn spectrum width is increased by a factor of 1.4 according to the relation $1/\cos(\alpha)$ (see the shift of the low energy edge of the Zn spectra). RBX fit of He^+-RBS spectra for the two different tilt angles accurately gives the layer thickness in units of atom/cm^2.

Fig. 4 shows p-EBS spectra of BeO and MgO co-alloyed ZnO layers Q3 and Q6, recorded for sample tilt angles of $\alpha = 7^o$ and $\alpha = 70^o$, respectively, together with the best fit

RBX simulations. Here the increased tilt angle is reflected in the rise of the Zn and Be peak intensity by a factor of 2.9, according to the relation $1/\cos(\alpha)$. Note, here the Al signal and the oxygen signal do not change significantly with the tilt angle because they come from the thick sapphire substrate (except a small oxygen peak from BeZnO/ZnO and BeMgZnO/ZnO). On the other hand, the small Mg peak is overshadowed by the Al background and it is difficult to identify. Some deviation of the simulated spectra from the measured ones at the oxygen edges can be observed which may be due to the interplay of the oxygen yield with the oscillating aluminum signal. However, such slight anomaly does not significantly affect the outcome of the evaluation procedure.

Fig. 5 shows the Be peak regions of p-EBS spectra for pure ZnO and for three BeMgZnO layers Q3, Q5, and Q6, measured at tilt angles of $\alpha = 7^{o}$ and 70^{o}, respectively. There is a good overall agreement between the measurements and simulations. A smooth signal character can be observed in Fig. 5(a) showing small statistical scattering on the background that originates from the sapphire substrate. The additional Be peaks in Fig. 5(b), (c), and (d) reside on the background shown in Fig. 5(a). Note, the uncertainty of Be analysis in p-EBS is determined not only by the Be atomic concentration but also by the thickness of the BeMgZnO layer, since both parameters have influence on the Be peak integral. The typical statistical uncertainty for the Be peak integral is ±20% for $\alpha = 7^{o}$ and ±7% for $\alpha = 70^{o}$ tilt. Another source of uncertainty considered in the recalculation of the Be content is the ±5% uncertainty of the given Be cross-section for protons $\sigma(Be)$ [21]. The total uncertainty can be calculated considering the uncertainties from both the Be peak integral and the Be cross-section. Note the uncertainty of the Mg content was considered as the statistical uncertainty of the background free Mg yield in the He^{+}-RBS spectra. All evaluated layer compositions together with the derived uncertainties of the Be and Mg contents are given in Table 2.

Note beside the layer composition and thickness RBS in combination with channeling (RBS/C) can also provide information about crystalline quality and the presence of interstitials [18]. Our preliminary He^{+}-RBS/C experiments (not shown) revealed good crystalline quality of the reference ZnO layer and the epitaxial growth of BeMgZnO on the ZnO seed. For instance *c*-axis RBS/C spectra of sample Q4 show significant drop of both the Mg and Zn yield as compared to the random yield thus suggesting mainly substitutional location of Mg in the BeMgZnO lattice. Detailed localization analysis for Be is challenging with He^{+}-RBS/C or p-EBS/C because of the small yield and/or high signal to background ratio in channeling conditions for Be located at substitutional lattice sites. The detailed analysis of interstitials and substitutional atoms in BeMgZnO requires careful multiaxial channeling experiments and angular scans [51] and is out of the scope of this paper.

The obtained Be and Mg concentrations and their uncertainties as input parameters were used to determine the band gap for each sample using HSE hybrid density functional calculations. Moreover, the optical bandgap energy (E_g) was estimated from the $(\alpha_{opt}h\nu)^2$ vs. $h\nu$ Tauc plots (Fig. 6(a)) where α_{opt}, the absorption coefficient was deduced from the transmission measurements and the measured thickness values. The calculated electronic and experimental optical (Tauc) bandgaps of the studied samples are compared in Fig 6(b). The errors on the *x*-axis show the uncertainty of the bandgap values extracted from optical transmittance experiments due to broadened absorption edges for BeZnO and BeMgZnO. The marked error bars on the *y*-axis represent the upper and lower limits of the calculated bandgaps due to the uncertainty in the Be and Mg concentration measurements as listed in Table 2. The obtained bandgaps for ternary and quaternary samples can be fitted by a linear function with a slope of 1.046(±0.059), see the red line. The offset between the fitted line and

one-to-one experiment-to-theory line (dashed line) varies between 0.31 and 0.37 eV as the Tauc bandgap increases.

Evidently the error on the *y*-axis in determining the Be and Mg concentrations is smaller than that due to other sources within the theoretical method used. For instance, the HSE hybrid functional was tuned to match the measured ZnO bandgap. The bandgaps of BeO and MgO are not perfectly matched within this functional; therefore, the uncertainty in the computed bandgaps increases with increasing content of Be and Mg. In addition, the zero point motion effects on the bandgap are absent in this method, while they are absorbed into the tuned bandgap of ZnO, and they may be different in BeO and MgO, thus introducing additional uncertainty. Finally, the crystal structures of BeMgZnO of different compositions were obtained from accurate relaxations of lattice parameters within the GGA approximation, known to overestimate lattice parameters in oxides by 1-2%.

Note, as in the case of most *ab-inito* methods, the HSE calculations do not include temperature effects while optical measurements were performed at room temperature. For ZnO the lowering of the measured excitonic bandgap by 68 meV was reported when increasing the temperature from 5 K to 295 K [45]. Also, the bandgap, measured in optical transmittance is lower by the exciton binding energy (being about 60 meV for ZnO) than the electronic bandgap obtained from HSE calculations. These factors can explain the offset of ~0.17 eV for ZnO found in this work. For MgZnO alloys exciton binding energies between 56 and 65 meV have been reported in the Mg content range of 6-23 atom % [45], while for BeO a value of 170 meV was found [52]. For BeZnO and BeMgZnO alloys this parameter probably falls within the range determined by ZnO and BeO. Consequently, the offset in Fig. 6(b) between theoretical and experimental bandgaps for BeZnO and BeMgZnO can be significantly reduced when considering exciton binding energies and temperature differences as discussed above.

In summary, Fig. 6(b) demonstrates adequate description of electronic properties of BeMgZnO alloys by the exchange tuned HSE hybrid functional theory. Furthermore, the remarkable agreement between measured and fitted He^+-RBS/p-EBS spectra as well as between measured optical bandgaps and calculated bandgaps provide a convincing justification of the demonstrated analytical method for the accurate compositional analysis of BeMgZnO thin films.

4. Conclusion

In this work a detailed atomic compositional, optical, and theoretical analysis of BeZnO and BeMgZnO alloys has been demonstrated.

Instead of previously applied analytical techniques like SIMS or XPS, which leads to sputtering and sample damage effects, require sample standards, and suffers from difficulties in the detection of the light Be element, we apply ion beam analysis as nondestructive characterization tool. Our concept is based on the non-Rutherford proton elastic backscattering reaction around 2.5 MeV proton energy where an enhancement factor of 60 in the cross-section of Be can be achieved as compared to the Rutherford value. To minimize uncertainties proton elastic backscattering was combined with He^+-RBS and detailed multiple spectrum fit evaluation procedure taking into account the actual cross-sections for backscattering, electronic stopping, and detection processes. With the combined IBA technique the composition and layer structure of wurtzite BeZnO/ZnO and BeMgZnO/ZnO systems grown on (0001) sapphire were determined with good accuracy down to Be content of 7 atom% with typical uncertainty of 1-2 atom%.

Based on the measured atomic composition of BeO and MgO co-alloyed ZnO layers, hybrid density functional bandgap calculations were performed and compared to experimental

optical bandgaps. A linear correlation between theory and experiment was found in the whole bandgap range studied from 3.26 eV to 4.62 eV for different Be and Mg contents.

The presented analytical concept should help facilitate bandgap engineering for potential applications of BeZnO and BeMgZnO alloys, like solar blind UV photodetectors or heterostructures for UV emitters and intersubband devices.

Acknowledgement

This research was funded by a grant from the Office of Scientific Research with Dr. J. Hwang and Dr. K. Goretta as the program monitor. Partial support from the project PiezoMAT FP7-ICT-2013-10-611019 is greatly appreciated. J. V. acknowledges the Senior Leaders & Scholars Fellowship grant of The Hungarian-American Enterprise Scholarship Fund (HAESF/CIEE).

References

[1] L. Su, Y. Zhu, Q. Zhang, M. Chen, T. Wu, X. Gui, B. Pan, R. Xiang, and Z. Tang, Appl. Surf. Sci., **274** (2013), p. 341

[2] P. Schreiber, T. Dang, T. Pickenpaugh, G. A. Smith, P. Gehred, and C. W. Litton, Proc. SPIE, **3629** (1999), p. 230

[3] L. Su, Y. Zhu, Q. Zhang, M. Chen, X. Ji, T. Wu, X. Gui, B. Pan, R. Xiang, and Z. Tang, J. Phys. D, **46** (2013), p. 245103

[4] A. Ohtomo, M. Kawasaki, T. Koida, K. Masubuchi, H. Koinuma, Y. Sakurai, Y. Yoshida, T. Yasuda, and Y. Segawa, Appl. Phys. Lett., **72** (1998), p. 2466

[5] A. K. Sharma, J. Narayan, J. F. Muth, C. W. Teng, C. Jin, A. Kvit, R. M. Kolbas, and O. W. Holland, Appl. Phys. Lett., **75** (1999), p. 3327

[6] X. L. Du, Z. X. Mei, Z. L. Liu, Y. Guo, T. C. Zhang, Y. N. Hou, Z. Zhang, Q. K. Xue, and A. Y. Kuznetsov, Adv. Mater., **21** (2009), p. 4625

[7] Q. Yan, P. Rinke, M. Winkelnkemper, A. Qteish, D. Bimberg, M. Scheffler, and C. G. Van de Walle, Appl. Phys. Lett., **101** (2012), p. 152105

[8] C. Yang, X. M. Li, Y. F. Gu, W. D. Yu, X. D. Gao, and Y. W. Zhang, Appl. Phys. Lett., **93** (2008), p. 112114

[9] C. Yang, X. M. Li, X. D. Gao, X. Cao, R. Yang, and Y. Z. Li, J. Cryst. Growth, **312** (2010), p. 978

[10] H. L. Shi and Y. Duan, Eur. Phys. J. B, **66** (2008), p. 439

[11] X. Su, P. Si, Q. Hou, X. Kong, and W. Cheng, Physica B, **404** (2009), p. 1794

[12] L. Su, Y. Zhu, M. Chen, Q. Zhang, Y. Su, X. Ji, T. Wu, X. Gui, R. Xiang, and Z. Tang, Appl. Phys. Lett., **103** (2013), p. 072104

[13] M. P. Seah, Surf. Interface Anal. **44** (2012) p. 497; http://physics.nist.gov/PhysRefData/Note/fig2.html

[14] W. J. Kim, J. H. Leem, M. S. Han, I.-W. Park, Y. R. Ryu, and T. S. Lee, J. Appl. Phys., **99** (2006), p. 096104

[15] Z. Zolnai, N. Nagy, A. Deák, G. Battistig, and E. Kótai, Phys. Rev. B, **83** (2011), p. 233302

[16] Z. Zolnai, Appl. Surf. Sci., **281** (2013), p. 17

[17] C. Jeynes, N. P. Barradas, and E. Szilágyi, Anal. Chem., **84** (2012), p. 6061; J. L. Colaux, and C. Jeynes, Anal. Methods, **6** (2014), p. 120

[18] Z. Zolnai, A. Ster, N. Q. Khánh, G. Battistig, T. Lohner, J. Gyulai, E. Kótai, and M. Posselt, J. Appl. Phys., **101** (2007), p. 023502

[19] E. Szilágyi, N. Q. Khánh, Z. E. Horváth, T. Lohner, G. Battistig, Z. Zolnai, E. Kótai, and J. Gyulai, Mater. Sci. Forum, **353-356** (2001), p. 271

[20] M. Allab, A. Boucenna, and M. Haddad, J. Phys. (Paris), **44**, (1983), p. 579 and references therein.

[21] J. A. Leavitt, L. C. Jr. McIntyre, R. S. Champlin, J. O. Jr. Stoner, Z. Lin, M. D. Ashbaugh, R. P. Cox, and J. D. Frank, Nucl. Instrum. Methods Phys. Res. B, **85** (1994) p. 37

[22] J. M. Khoshman, D. C. Ingram, and M. E. Kordesch, J. Non-Cryst. Solids, **354** (2008), p. 2783

[23] E. Kótai, Nucl. Instrum. Methods Phys. Res. B, **85** (1994), p. 588

[24] N. P. Barradas, K. Arstila, G. Battistig, M. Bianconi, N. Dytlewski, C. Jeynes, E. Kótai, G. Lulli, M. Mayer, E. Rauhala, E. Szilágyi, and M. Thompson, Nucl. Instrum. Methods Phys. Res. B, **262** (2007), p. 281

[25] N. P. Barradas et al, Nucl. Instrum. Methods Phys. Res. B, **247** (2008), p. 381

[26] Mayer et al, Nucl. Instrum. Methods Phys. Res. B, **332** (2014) p. 176

[27] M. Toporkov, V. Avrutin, S. Okur, N. Izyumskaya, D. Demchenko, J. Volk, D. J. Smith, H. Morkoç, and Ü. Özgür, J. Cryst. Growth, **402** (2014), p. 60

[28] F. Pászti, A. Manuaba, C. Hajdu, A. A. Melo, and M. F. Da Silva, Nucl. Instrum. Methods Phys. Res. B, **47** (1990), p. 187

[29] Y. G. Mashkarov, A. S. Deineko, R. P. Slabospitskii, I. I. Zalyubovskii, Izv. Akad. Nauk. SSSR Ser. Fiz., **40** (1976), p. 1218

[30] R. A. Laubenstein, M. J. W. Laubenstein, L. J. Koester, and R. C. Mobley, Phys. Rev., **84** (1951), p. 12

[31] R. Amirikas, D. N. Jamieson, S. P. Dooley, Nucl. Instrum. Methods Phys. Res. B, **77** (1993), p. 110

[32] F. P. Mooring, L. J. Koester Jr., E. Goldberg, D. Saxon, and S. G. Kaufmann, Phys. Rev., **84** (1951), p. 703

[33] E. Rauhala, Nucl. Instrum. Methods Phys. Res. B, **40/41** (1989), p. 790

[34] Li Gong-ping, Zhang Xiao-dong, Xu Jin-zhang, and Liu Zheng-min, J. Radioanal. Nucl. Chem., **250** (2001), p. 555

[35] M. Chiari, L. Giuntini, P. A. Mandó, N. Taccetti, Nucl. Instrum. Methods Phys. Res. B, 1**74** (2001), p. 259

[36] Handbook of modern ion beam materials analysis, edited by J. R. Tesmer, and M. Nastasi, MRS Pittsburgh, Pennsylvania, USA, 1995

[37] A. F. Gurbich, Nucl. Instrum. Methods Phys. Res. B, **129** (1997), p. 311

[38] A. F. Gurbich, C. Jeynes, Nucl. Instrum. Methods Phys. Res. B, **265** (2007), p. 447

[39] A. F. Gurbich, Nucl. Instrum. Methods Phys. Res. B, **268** (2010), p. 1703

[40] www-nds.iaea.org/exfor/ibandl.htm

[41] J. Heyd, G. E. Scuseria, and M Ernzerhof, J. Chem. Phys., **118** (2003), p. 8207

[42] G. Kresse and J. Furthmüller, Phys. Rev. B, **54** (1996), p. 11169

[43] P. E. Blöchl, Phys. Rev. B, **50** (1994), p. 17953

[44] G. Kresse and D. Joubert, Phys. Rev. B, **59** (1999), p. 1758

[45] M. D. Neumann, C. Cobet, N. Esser, B. Laumer, T. A. Wassner, M. Eickhoff, M. Feneberg, and R. Goldhahn, J. Appl. Phys., **110** (2011), p. 013520

[46] D. C. Reynolds, D. C. Look, B. Jogai, C. W. Litton, G. Cantwell, and W. C. Harsch, Phys. Rev. B., **60** (1999), p. 2340

[47] Y. R. Ryu, T. S. Lee, J. A. Lubguban, A. B. Corman, H. W. White, J. H. Leem, M. S. Han, Y. S. Park, C. J. Youn, and W. J. Kim, Appl. Phys. Lett., **88** (2006), p. 052103

[48] J. H. Yu, J. H. Kim, H. J. Yang, T. S. Kim, T. S. Jeong, C. J. Youn, and K. J. Hong, J. Mater. Sci., **47** (2012), p. 5529

[49] R. C. Whited, C. J. Flaten, and W. C. Walker, Solid State Commun., **13** (1973), p. 1903

[50] http://www.srim.org

[51] E. Szilágyi, T. Becze-Deák, L. Bottyán, A. Kocsonya, E. Kótai, D. L. Nagy, A. Kling, G. Battistig, N. Q. Khánh, and K. Polgár, Solid State Commun., **115** (2000), p. 535

[52] D. M. Roessler, and W. C. Walker, J. Phys. Chem. Solids, **30** (1969), p. 157

Figure captions

Fig. 1. (Color online) Cross-section vs. ion energy data for (a) Rutherford backscattering of He^+ and (b) non-Rutherford elastic backscattering of H^+on Be [29], O [31], Mg [32], Al [33, 34], and Zn [36], used in the spectrum evaluation procedure. Gray stripes show the energy lost by (a) 1 MeV He^+ and (b) 2.53 MeV H^+ projectiles through electronic stopping when crossing a 150 nm-thick ZnO layer.

Fig. 2. (Color online) (a) 1 MeV He^+ RBS spectra of ZnO, BeZnO (T), and BeMgZnO (Q1, Q3, Q4, Q6) layers and (b) 2.53 MeV H^+ non-Rutherford elastic backscattering spectrum of BeMgZnO (Q2), grown on sapphire. In panel (b) the simulated spectrum is also shown by the red line. Surface edges for Be, O, Mg, and Zn, and the spectrum edge for buried Al (in sapphire) are indicated. Depth scales for Zn are also shown. Inset: schematics of the experiment and the sample structure used in the spectrum evaluation procedure.

Fig. 3. (Color online) 1 MeV He^+ RBS spectra of (a) ZnO and BeMgZnO (Q3), and of (b) BeZnO (T) and BeMgZnO (Q5) layers measured at sample tilt angles of $\alpha = 7^o$ and $\alpha = 45^o$, respectively. Surface edges for O, Mg, and Zn, and the spectrum edge for buried Al (in sapphire), as well as the depth scale for Zn are indicated. The symbols represent measured data. Simulated spectra by green and red lines are also shown.

Fig. 4. (Color online) 2.53 MeV non-Rutherford proton elastic backscattering spectra of BeMgZnO layers (a) Q3 and (b) Q6 measured at sample tilt angles of $\alpha = 7^o$ and $\alpha = 70^o$, respectively. Surface peaks for Be, Mg, and Zn, and spectrum edges for O and buried Al (in sapphire), as well as the depth scale for Zn are indicated. The symbols represent measured data. Simulated spectra by red and blue lines are also shown.

Fig. 5. (Color online) Beryllium peak regions of 2.53 MeV non-Rutherford proton elastic backscattering spectra for (a) ZnO, and BeMgZnO layers (b) Q3, (c) Q5, and (d) Q6, respectively, measured at sample tilt angles of $\alpha = 7^o$ and $\alpha = 70^o$. The symbols represent measured data. Simulated spectra by red and blue lines are also shown.

Fig. 6. (Color online) (a) Tauc plots of absorption edges deduced from transmittance measurements and (b) comparison of the experimental optical and calculated bandgaps for the studied ZnO, BeZnO (T), and BeMgZnO (Q1-Q6) samples. Hybrid density functional calculations are based on Mg and Be concentrations extracted from 1 MeV He^+-RBS and 2.53 MeV p-EBS analysis. The solid red line is the linear fit to red dots. The dashed line shows the one-to-one function.

Table 1.
Energy, electronic stopping power (S_e,), and enhancement factors for crosssections with respect to the Rutherford value (σ/σ_R) for the analyzing He^+ and H^+ ions. S_e values are calculated with SRIM [50] simulations for stopping in pure ZnO.

Ion	**Energy (keV)**	**S_e (eV/nm)**	**Cross section enhancement factor σ/σ_R**				
			Be	O	Mg	Al	Zn
He^+	1000	420	1	1	1	1	1
H^+	2530	45	60	5.9	1.67	~1 oscillation	1

Table 2.
Atomic compositions (Be and Mg concentrations in at. % substitution of Zn atoms), thicknesses for the BeZnO or BeMgZnO layer (t_{layer}) and for the buffer ZnO layer (t_{buffer}) determined from ion beam analysis, together with *c*-lattice parameters, experimental optical (E_g exp.), and calculated bandgaps (E_g calc.) of the studied samples.

Sample	Composition		t_{layer}		t_{buffer}		*c* (Å)	E_g exp. (eV)	E_g calc. (eV)
	Be conc. (at. %)	Mg conc. (at. %)	(10^{17} at./cm^2)	(nm)	(10^{17} at./cm^2)	(nm)			
ZnO			19	229.2	-	-	5.20	3.26	3.43
T	8(±0.98)		12	142.5	-	-	5.123	3.34	3.58(±0.03)
Q1	11(±1.19)	14(±0.32)	7.5	88.7	1.1	13.3	5.099	3.66	4.09(±0.02)
Q2	8(±0.82)	30(±0.36)	11.2	131.5	0.5	6	5.063	4.01	4.35(±0.02)
Q3	7(±0.75)	33(±0.33)	13.7	160.3	1.5	18	5.049	4.06	4.41(±0.02)
Q4	7(±0.69)	46(±0.37)	14.7	171.3	1.2	14.5	5.027	4.41	4.68(±0.02)
Q5	19(±1.85)	42(±0.55)	7.2	82.4	0.9	10.9	4.939	4.62	5.01(±0.06)
Q6	12(±1.44)	52(±0.57)	7.8	90	1.8	21.7	4.979	4.62	5.01(±0.05)

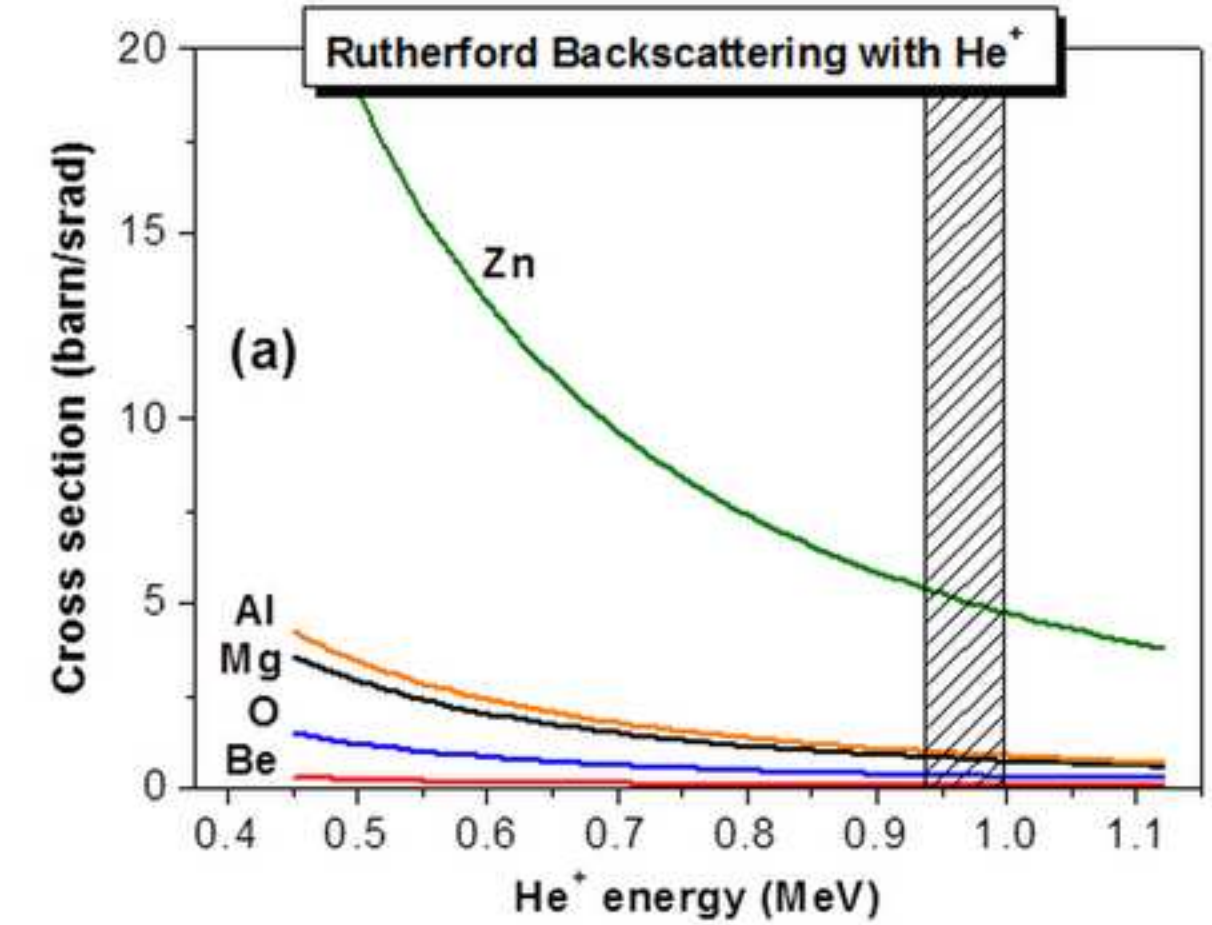

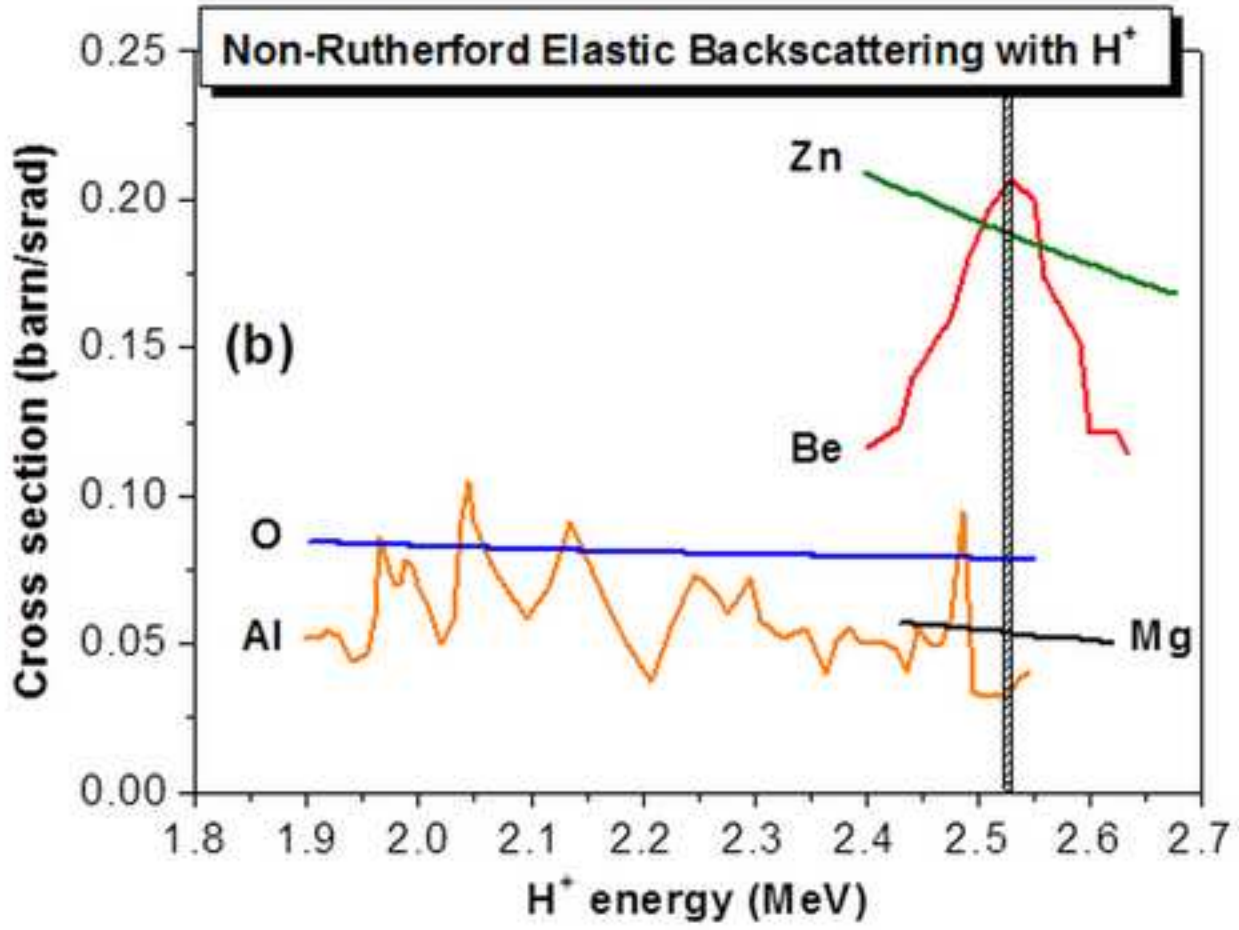

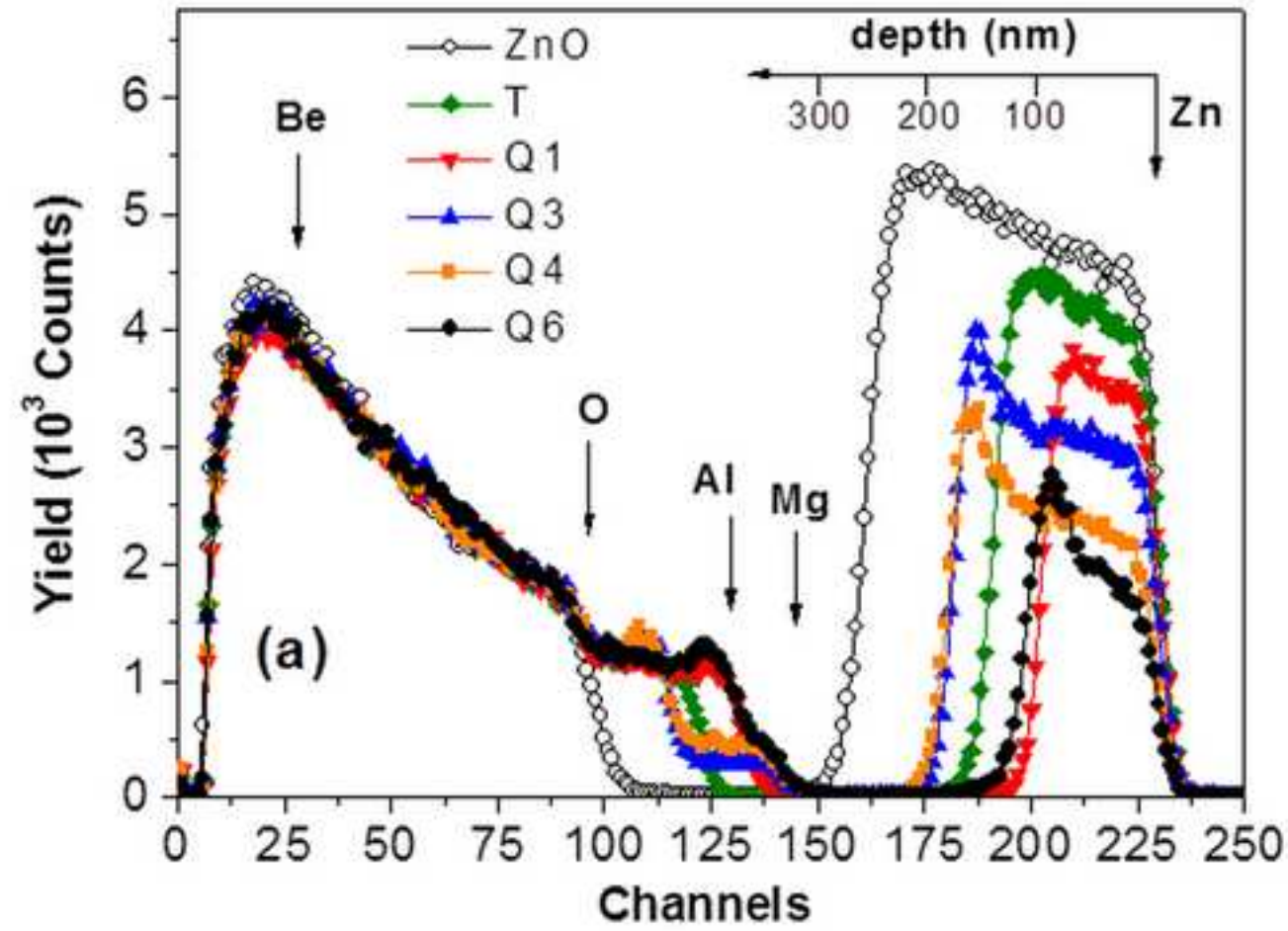

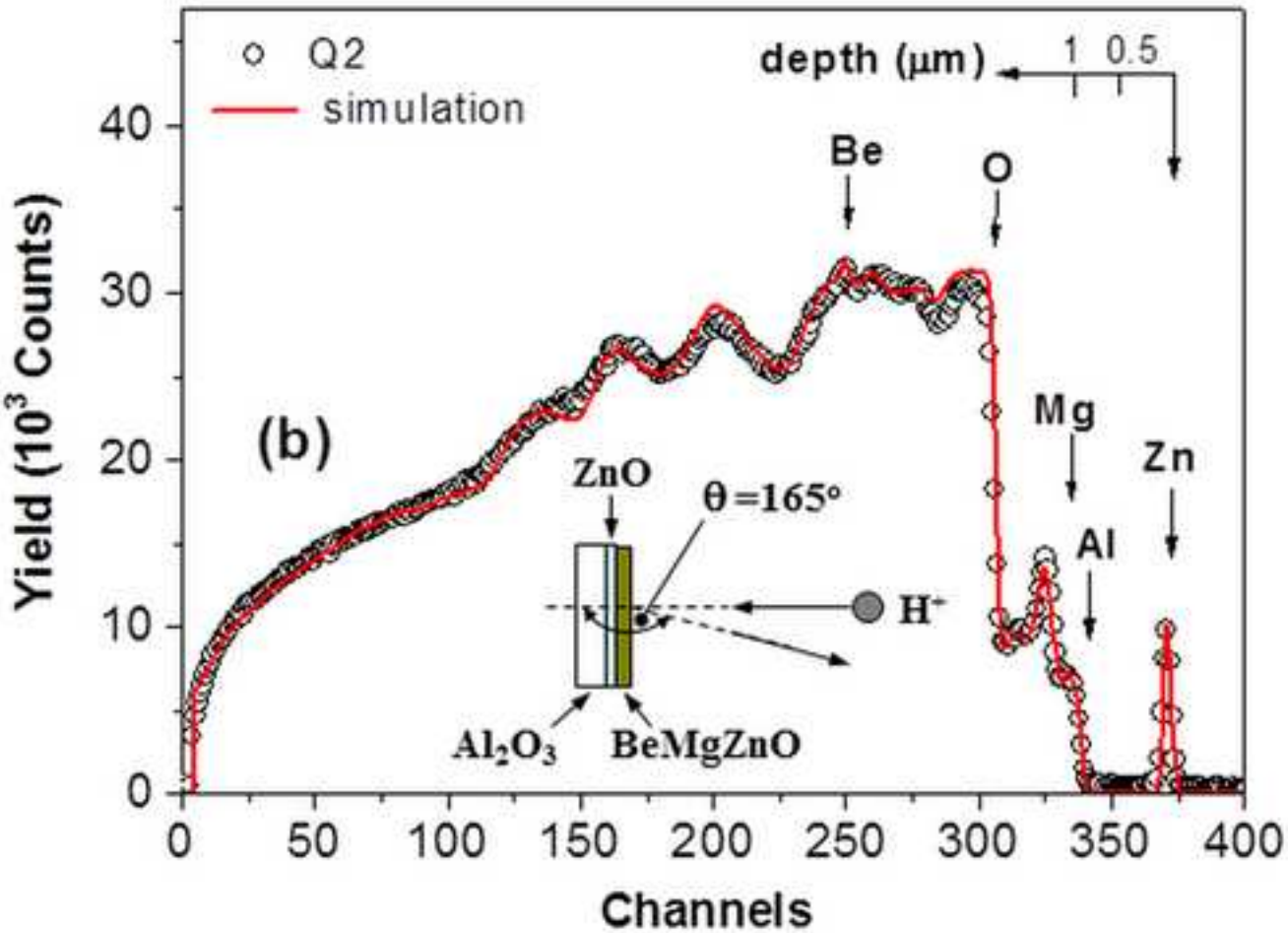

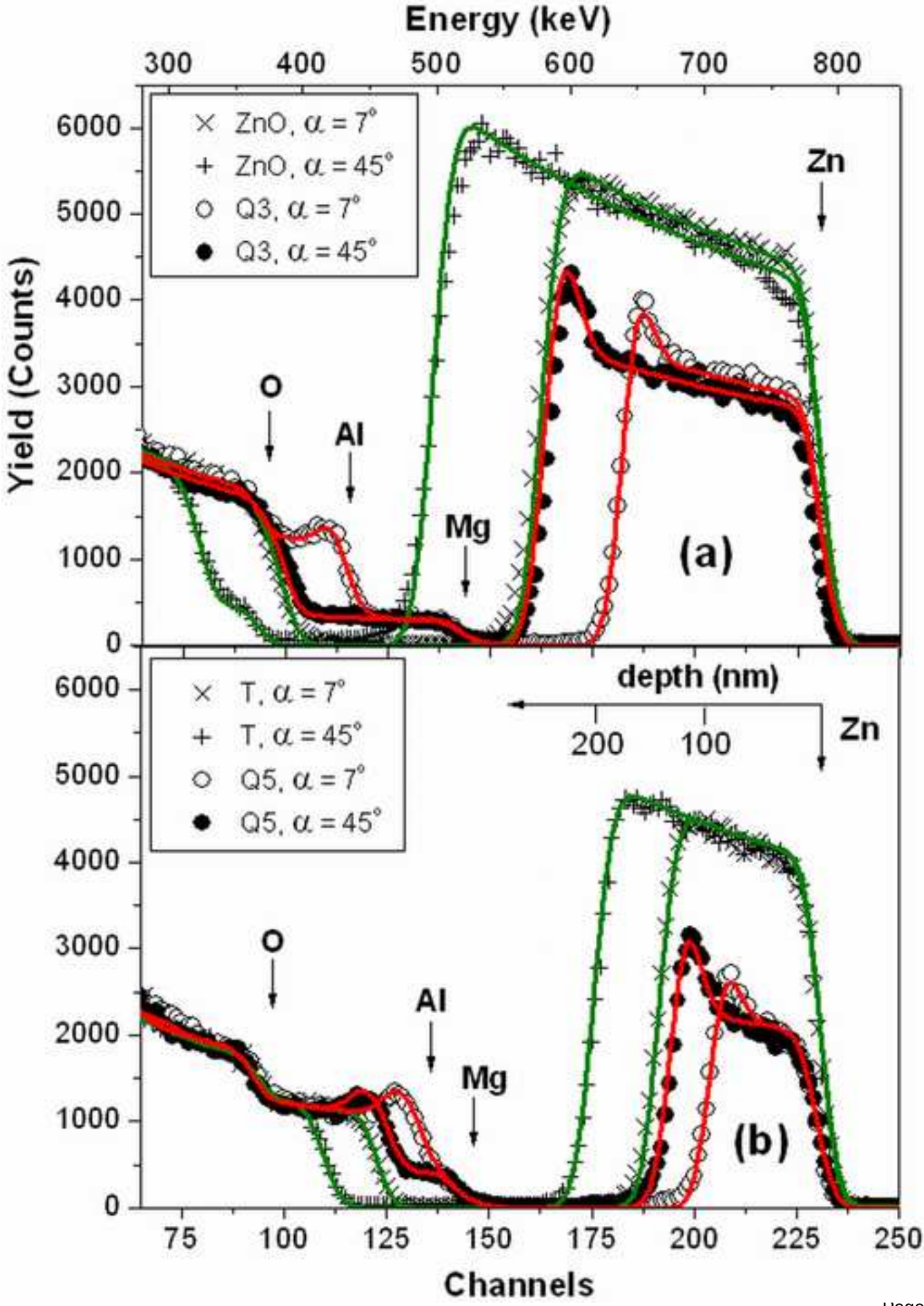

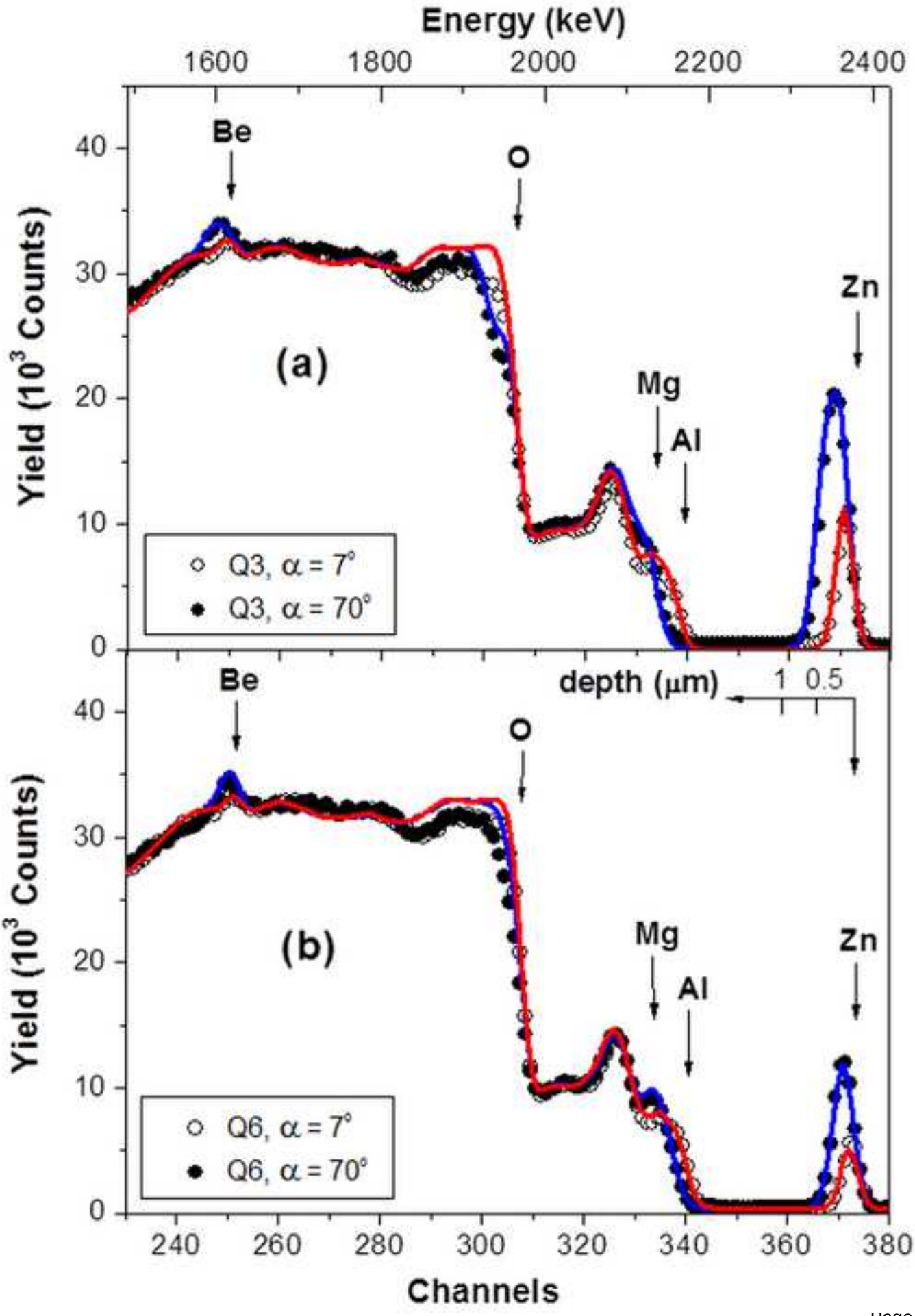

Figure5

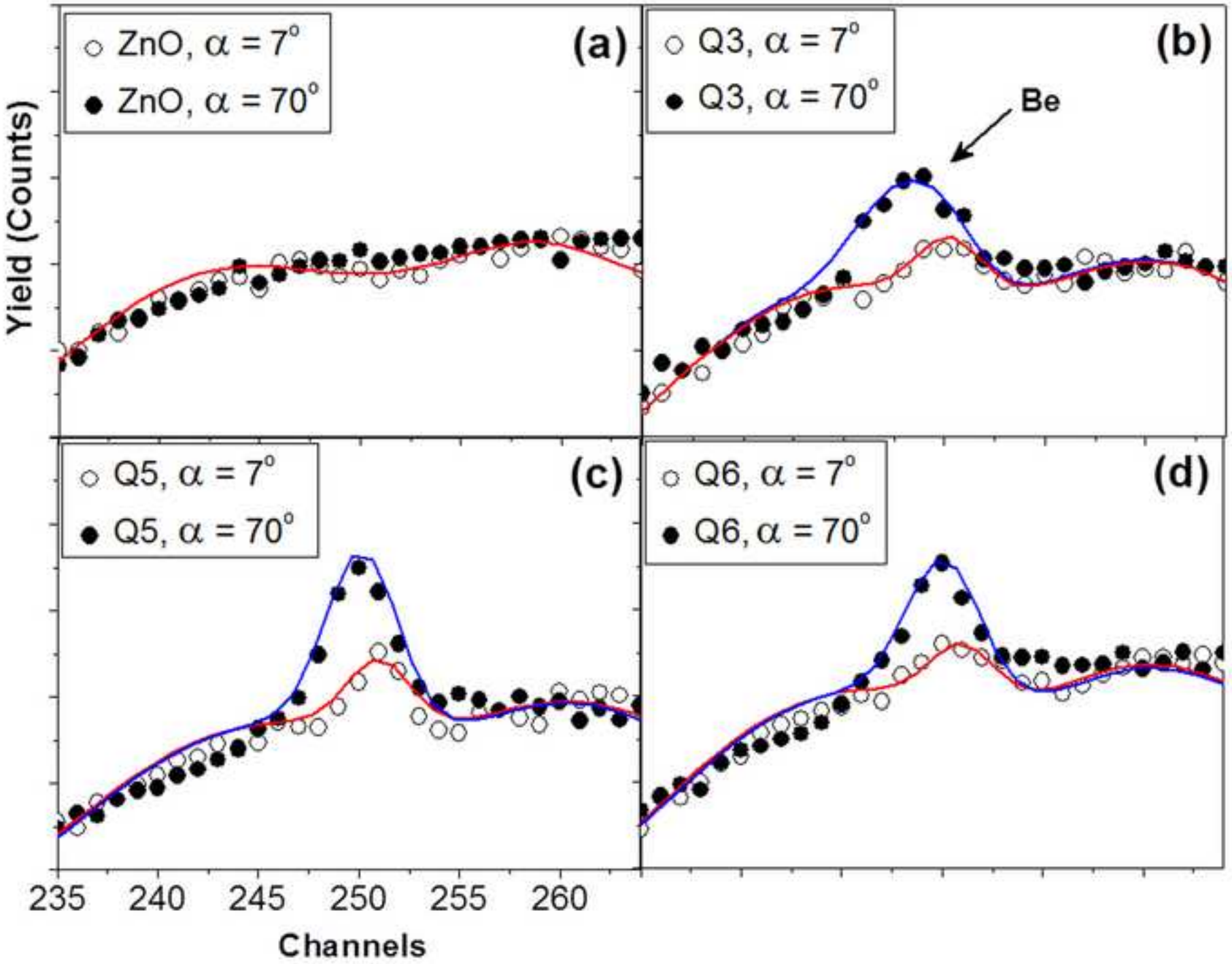
ZnO, α = 7°
ZnO, α = 70°
(a)
Q3, α = 7°
Q3, α = 70°
Be
(b)
Q5, α = 7°
Q5, α = 70°
(c)
Q6, α = 7°
Q6, α = 70°
(d)
Yield (Counts)
235
240
245
250
255
260
Channels